



Effects of $\text{Na}_2\text{B}_4\text{O}_7 \cdot 10\text{H}_2\text{O}$ on microstructure and mechanical properties of AlSi7Mg0.3 and AlSi10MnMg alloys

Jaehui Bang¹ · Eungsun Byon[†] · Eunkyung Lee^{††}

(Received November 22, 2021 ; Revised December 8, 2021 ; Accepted December 21, 2021)

Abstract: Iron contained in aluminum alloys is an impurity that cannot be removed, and it causes porosity in the solidification process and forms intermetallic compounds, which negatively affects mechanical characteristics; therefore, Fe intermetallic compound control is required. Therefore, in this study, an analysis of the microstructure and mechanical properties of aluminum alloys produced by injecting $\text{Na}_2\text{B}_4\text{O}_7 \cdot 10\text{H}_2\text{O}$ with a maximum solubility of hydrogen was conducted. After the addition of $\text{Na}_2\text{B}_4\text{O}_7 \cdot 10\text{H}_2\text{O}$, the size of the Fe-rich intermetallic AlSi7Mg0.3 compound reduced, and the needle-shaped Fe intermetallic phase transformed into Chinese-script-shaped in the AlSi10MnMg alloy. Further, the fraction of the Fe intermetallic compounds reduced by 0.17 % and 0.15 % in AlSi7Mg0.3 and AlSi10MnMg , respectively, after the addition of $\text{Na}_2\text{B}_4\text{O}_7 \cdot 10\text{H}_2\text{O}$, and the secondary dendrite arm spacing and size of the Si particles increased. In the alloys with the addition of $\text{Na}_2\text{B}_4\text{O}_7 \cdot 10\text{H}_2\text{O}$, the increased secondary dendrite arm spacing and blocky Si reduced the tensile strength of the AlSi7Mg0.3 and AlSi10MnMg alloys to 11.45 MPa and 11.78 MPa, respectively. In contrast, the transformed Fe intermetallic compounds increased the hardness of the Al matrix to 4 HV and 2.53 HV in AlSi7Mg0.3 and AlSi10MnMg alloys, respectively.

Keywords: $\text{Na}_2\text{B}_4\text{O}_7 \cdot 10\text{H}_2\text{O}$, Fe intermetallic compound, AlSi7Mg0.3 , AlSi10MnMg , Microstructure

1. Introduction

Commercially pure aluminum is an extremely flexible metal with low strength, and is not used for structural applications [1]; however, it is utilized by alloying with Si, Mg, Cu, Zn, etc. [2]-[5]. Casting defects, such as intermetallic compounds and porosity occur during casting when an alloying element is added to a master alloy [6]-[8]. Casting defects must be eliminated because they are a major cause of unexpected damage and fracture, negatively affecting the quality of the cast product [9]-[11].

Fe is an impurity that cannot be removed from pure aluminum has a very low solid solubility of up to 0.05 % in aluminum [12] and is bonded with Si, Mn, or it is precipitated as an intermetallic compound with brittleness [13]-[14]. Brittle plate-like Fe intermetallic compounds act as nucleation sites for porosity [15], preferential corrosion attack, or as stress concentration and weak

points [16]-[18], negatively affecting the mechanical properties of castings. The needle-shaped Fe-rich intermetallic and porosity have a problem with AlSi7Mg0.3 and AlSi10MnMg alloys containing 0.2 % or less of Fe in an Al-Si-based alloy that occupies most of the casting alloys [19]-[21]. To circumvent these casting defects, degassing and flux processes [22] or heat treatments are performed to transform the shape of the Fe intermetallic compounds or the cast alloy is re-dissolved in the Al matrix [23].

When $\text{Na}_2\text{B}_4\text{O}_7 \cdot 10\text{H}_2\text{O}$ is used as hydrogen [13]-[14], [24] or aluminum brazing fluxes [25], and as an electrolytic solution for the plasma electrolyte oxidation (PEO) processes [26], Na and B components are added for eutectic Si and grain refinement [27]-[28], respectively, but they cause porosity due to the O component. However, previous studies have shown that $\text{Na}_2\text{B}_4\text{O}_7 \cdot 10\text{H}_2\text{O}$ reduces the iron contents from 0.14 wt.% to 0.1

^{††} Corresponding Author (ORCID: <http://orcid.org/0000-0003-0723-8524>): Assistant Professor, Interdisciplinary Major of Maritime AI Convergence, Department of Ocean Advanced Materials Convergence Engineering, Korea Maritime & Ocean University, 727, Taejong-ro, Yeongdo-gu, Busan 49112, Korea, E-mail: elee@kmou.ac.kr, Tel: 051-410-4353

[†] Co-Corresponding Author (ORCID: <http://orcid.org/0000-0002-5145-3339>): Ph. D., Surface Materials Division, Department of Extreme Environmental Coatings, Korea Institute of Materials Science, 797, Changwon-daero, Seongsan-gu, Chanwon 51508, Korea, E-mail: esbyon@kims.re.kr, Tel: 055-280-3555

1 M. S. Candidate, Interdisciplinary Major of Maritime AI Convergence, Department of Ocean Advanced Materials Convergence Engineering, Korea Maritime & Ocean University, E-mail: bbbb_9797@naver.com, Tel: 051-410-4955

This is an Open Access article distributed under the terms of the Creative Commons Attribution Non-Commercial License (<http://creativecommons.org/licenses/by-nc/3.0>), which permits unrestricted non-commercial use, distribution, and reproduction in any medium, provided the original work is properly cited.

wt.% and 0.33 wt.% to 0.18 wt.%, i.e. by more than 45 % in pure aluminum [13]-[14]. Despite the positive effects of $\text{Na}_2\text{B}_4\text{O}_7 \cdot 10\text{H}_2\text{O}$, studies on the effects of aluminum alloys on iron intermetallic compounds and microstructures are insufficient. In addition, aluminum alloys produce numerous intermetallic compounds than pure aluminum [20], therefore, to analyze the effects of $\text{Na}_2\text{B}_4\text{O}_7 \cdot 10\text{H}_2\text{O}$ on aluminum alloys further studies are required. In this study, $\text{Na}_2\text{B}_4\text{O}_7 \cdot 10\text{H}_2\text{O}$ was used to confirm the intermetallic compounds formed by the maximum hydrogen solubility in aluminum alloys, to analyze the mechanical properties, and to control the microstructures to collect data for $\text{Na}_2\text{B}_4\text{O}_7 \cdot 10\text{H}_2\text{O}$ applications.

2. Experimental Methods

2.1. Materials

AlSi7Mg0.3 and AlSi10MnMg alloys were used to investigate the effects of the hydrogen flux on aluminum alloys.

The chemical composition of AlSi7Mg0.3 alloy is 7.06 wt.% Si, 0.36 wt.% Mg, 0.02 wt.% Mn, 0.13 wt.% Fe, 0.06 wt.% Cu, 0.09 wt.% Ti, and 92.28 wt.% Al. Few other chemical elements constituted less than 0.01 wt.% (Ni, Cr, Pb). The chemical composition of AlSi10MnMg alloy is 10.11 wt.% Si, 0.32 wt.% Mg, 0.6 wt.% Mn, 0.06 wt.% Fe, 0.08 wt.% Ti, 0.02 wt.% Sr, and 88.81 wt.% Al. Few other chemical elements in AlSi10MnMg alloy constituted less than 0.01 wt.% (Cu, Cr, Ni, Pb). $\text{Na}_2\text{B}_4\text{O}_7 \cdot 10\text{H}_2\text{O}$ hydrogen flux with a maximum hydrogen solubility of 24.08 ppm was added to the aluminum alloy. The alloy was dissolved at a temperature of 800 °C, and $\text{Na}_2\text{B}_4\text{O}_7 \cdot 10\text{H}_2\text{O}$ was added after 30 min of degassing, followed by stirring for 5 min, and then injected into the mold.

2.2 Thermodynamic simulations

The thermodynamic calculations of intermetallic compounds produced in the range of 25–800 °C were performed using JmatPro® software, on as-cast AlSi7Mg0.3, as-cast AlSi10MnMg, AlSi7Mg0.3 alloys with $\text{Na}_2\text{B}_4\text{O}_7 \cdot 10\text{H}_2\text{O}$, and AlSi10MnMg alloys with $\text{Na}_2\text{B}_4\text{O}_7 \cdot 10\text{H}_2\text{O}$. The intermetallic compounds were produced with AlSi7Mg0.3 and AlSi10MnMg alloys.

2.3. Microstructure analysis

The specimens were polished using SiC polishing papers of up to #2400 grit to observe the microstructure of the alloy. In

addition, the specimens were polished using a 0.25 μm diamond and a 0.04 μm colloidal suspensions. The porosity area fraction of the reduced pressure test specimens, microstructure and secondary dendrite arm spacing of the pretreated specimen, and fracture surfaces were examined by field emission scanning electron microscopy (FE-SEM; MIRA3, Tescan) with an accelerating voltage of 15.0 kV and using an optical microscope. To analyze the crystal structure of the as-cast and $\text{Na}_2\text{B}_4\text{O}_7 \cdot 10\text{H}_2\text{O}$ -added alloys, X-ray diffraction (XRD, D/MAX 2500 VL/PC, Rigaku) analysis was performed in the range of 20°–90° using Cu K α radiation, operating at 40 kV and 30 mA.

2.4. Mechanical property analysis

The mechanical properties of the alloys were evaluated to measure the tensile strength, yield strength, elongation, and hardness. A tensile test piece was prepared according to the ASTM E8 sub-size sheet tensile test.

The tensile test of each specimen was conducted for four trials using a UNIVERSAL TESTING MACHINE KDMT-156 at a cross-head rate of 1 mm/min. For the micro hardness test, an HM-122 hardness test machine (Akashi Co., Tokyo, Japan) was used, and the load was set to 1 N with an indentation time of 10 s, and the hardness of the specimens was recorded for 10 trials each.

3. Results and Discussion

3.1 Thermodynamic simulations

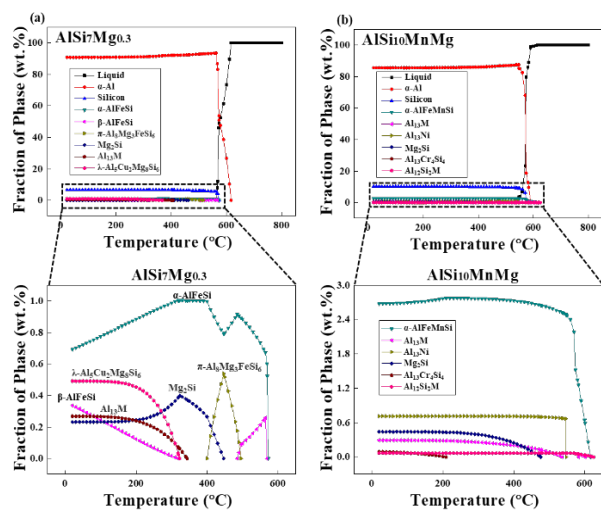


Figure 1: The phase fraction of (a) AlSi7Mg0.3 and (b) AlSi10MnMg, shown using the solidification behavior simulation of JmatPro® software

Figure 1 shows the thermodynamic simulation of the ASTM AlSi7Mg0.3 and AlSi10MnMg alloys calculated using the JmatPro software program. When analyzing the solidification behavior of each alloy based on **Figure 1**, the formation of the α -Al phase begins at approximately 600 °C in the AlSi7Mg0.3 alloy. As the solidification proceeded, a monovalent reaction of $L \rightarrow \alpha\text{-Al} + \text{Si}$ proceeded at approximately 570 °C, and $\beta\text{-AlFeSi}$ was formed from the reaction $L \rightarrow \alpha\text{-Al} + \text{Si} + \beta\text{-AlFeSi}$. Therefore, the phase fraction decreases in the order of $\alpha\text{-Al}_8\text{Fe}_2\text{Si}$ to $\text{Al}_5\text{Cu}_2\text{Mg}_8\text{Si}_6$, $\beta\text{-Al}_5\text{FeSi}$, Mg_2Si , and Al_3M . The AlSi10MnMg alloy formed an α -Al phase at 600 °C, and a monovalent reaction progressed at 570 °C. A considerable amount of $\alpha\text{-AlFeMnSi}$ is formed; however, the fractions of Al_{13}Ni , Mg_2Si , Al_3M , $\text{Al}_{13}\text{Cr}_4\text{Si}_4$, and $\text{Al}_{12}\text{Si}_2\text{M}$ phases are reduced. In Al_3M and $\text{Al}_{12}\text{Si}_2\text{M}$, M denotes a transition metal in the thermodynamic simulations of AlSi7Mg0.3 and AlSi10MnMg alloys. Transition elements such as Fe, Cu, Mn, Ni, and Zn are less soluble, and most of them precipitate.

3.2 Microstructure of aluminum alloys

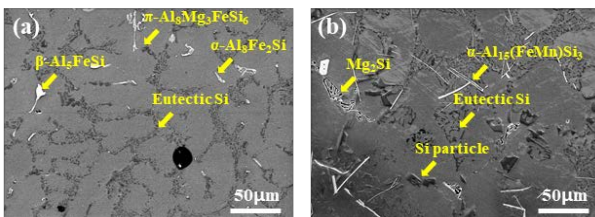


Figure 2: Microstructures of as-cast AlSi7Mg0.3 and AlSi10MnMg

The microstructure and intermetallic compounds of the alloy before and after the addition of Na₂B₄O₇·10H₂O were examined using FE-SEM and energy-dispersive spectroscopy (EDS) to compare the theoretically calculated intermetallic compounds through JmatPro with the produced phases, as shown in **Figure 2**.

In **Figure 2**, the presence of the α -Al matrix, eutectic Si, $\alpha\text{-Al}_{15}(\text{FeMn})\text{Si}_3$, $\beta\text{-Al}_5\text{FeSi}$, and $\alpha\text{-Al}_8\text{Fe}_2\text{Si}$ phases were confirmed, and $\pi\text{-Al}_8\text{Mg}_3\text{FeSi}_6$ that should disappear at 400 °C was observed for AlSi7Mg0.3. In AlSi7Mg0.3 and AlSi10MnMg alloys, dendrites, a typical casting microstructure, were observed, and in addition, α -Al dendrites and fine Al-Si eutectic phases were identified. In particular, needle-shaped $\beta\text{-Al}_5\text{FeSi}$ and $\alpha\text{-Al}_{15}(\text{FeMn})\text{Si}_3$ were observed in AlSi7Mg0.3 and AlSi10MnMg, respectively. These needle-shaped intermetallic compounds have a negative effect on the mechanical properties by causing

brittleness due to their weak bonding force with the matrix [15]-[18]. Further, Cu, Ni, and Cr intermetallic compounds which are present in **Figure 1** are not observed in **Figure 2** because they are present only in negligible amounts in AlSi7Mg0.3 and AlSi10MnMg alloys.

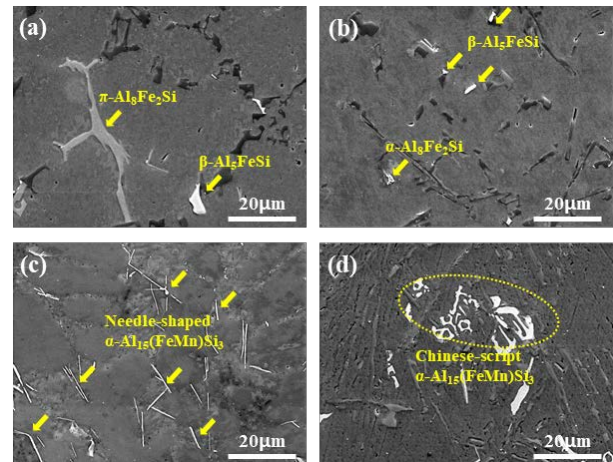


Figure 3: SEM images (magnified 3,000 \times) of (a) as-cast AlSi7Mg0.3, (c) as-cast AlSi10MnMg, (b) AlSi7Mg0.3 with Na₂B₄O₇, and (d) AlSi10MnMg with Na₂B₄O₇

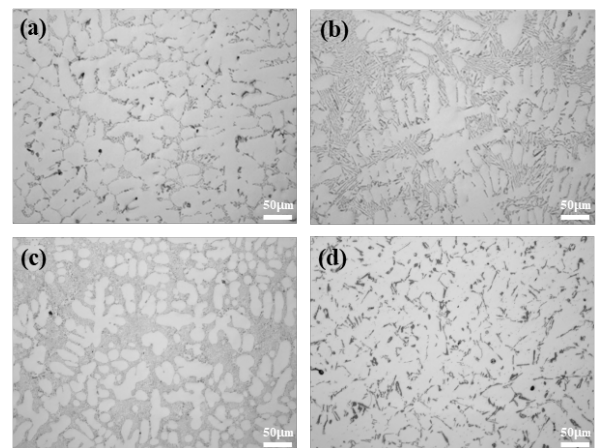


Figure 4: SEM images (magnified 200 \times) of (a) as-cast AlSi7Mg0.3, (c) as-cast AlSi10MnMg, (b) AlSi7Mg0.3 with Na₂B₄O₇, and (d) AlSi10MnMg with Na₂B₄O₇

However, as shown in **Figure 3**, the size of $\beta\text{-Al}_5\text{SiFe}$ decreased after the addition of Na₂B₄O₇·10H₂O. In the case of AlSi10MnMg, the needle shaped $\alpha\text{-Al}_{15}(\text{FeMn})\text{Si}_3$ was converted to Chinese-script Chinese-script compound, which indicates that the structure modified through the heat-treatment process [23].

Figure 4 shows the microstructure of the aluminum alloys observed using an optical microscope and shows the secondary

dendrite arm before and after the addition of $\text{Na}_2\text{B}_4\text{O}_7 \cdot 10\text{H}_2\text{O}$. AlSi7Mg0.3 with $\text{Na}_2\text{B}_4\text{O}_7$, and AlSi10MnMg with $\text{Na}_2\text{B}_4\text{O}_7$ have blocky coarsened Si compared to the as-cast alloy.

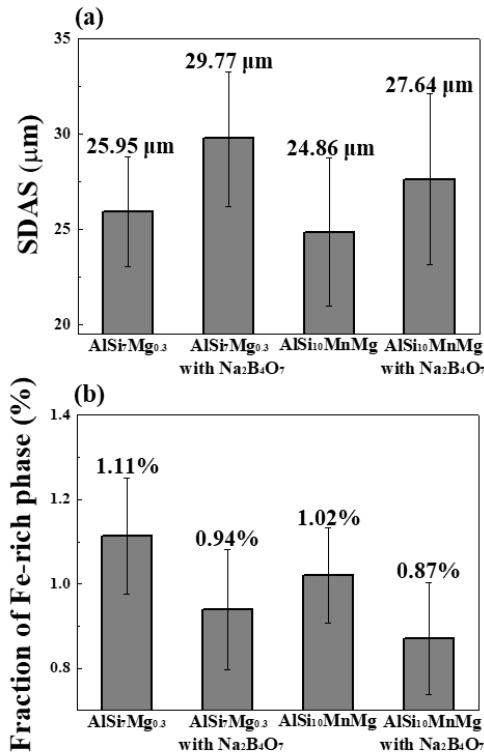


Figure 5: (a) Secondary dendrite arm spacing and (b) fraction of Fe-rich intermetallic phases of as-cast AlSi7Mg0.3 , as-cast AlSi10MnMg , and alloys with the addition of $\text{Na}_2\text{B}_4\text{O}_7$

Table 1: Area fractions and sphericity of eutectic Si in as-cast AlSi7Mg0.3 , as-cast AlSi10MnMg , and alloys with the addition of $\text{Na}_2\text{B}_4\text{O}_7$

Alloys	Eutectic Si		Sphericity
	as-cast	Area Fraction (%)	
AlSi7Mg0.3	as-cast	11.97 (± 2.12)	0.805 (± 0.04)
	with $\text{Na}_2\text{B}_4\text{O}_7$	12.15 (± 1.12)	0.795 (± 0.04)
AlSi10MnMg	as-cast	12.18 (± 1.18)	0.824 (± 0.02)
	with $\text{Na}_2\text{B}_4\text{O}_7$	12.53 (± 2.01)	0.752 (± 0.03)

From **Figure 5(a)**, the AlSi7Mg0.3 alloy has secondary dendrite arm spacing of $25.95 (\pm 2.88) \mu\text{m}$; however, it increased to $29.77 (\pm 3.53) \mu\text{m}$ when $\text{Na}_2\text{B}_4\text{O}_7$ is added, and in AlSi10MnMg with $\text{Na}_2\text{B}_4\text{O}_7$, the SDAS value increased from $24.86 (\pm 3.88) \mu\text{m}$ to $27.64 (\pm 4.49) \mu\text{m}$. In addition, from **Figure 5(b)**, adding $\text{Na}_2\text{B}_4\text{O}_7$ to AlSi7Mg0.3 reduced the fraction of Fe intermetallic compounds from $1.11\% (\pm 0.33\%)$ to $0.94\% (\pm 0.24\%)$, and in

the case of AlSi10MnMg , the fraction decreased from $1.02\% (\pm 0.31\%)$ to $0.87\% (\pm 0.23\%)$. Further, B in $\text{Na}_2\text{B}_4\text{O}_7$ was bound to Fe and precipitated into another phase of Fe_2B [13]-[14]; therefore, the fractions of Fe intermetallic compounds of $\beta\text{-AlFeSi}$, $\alpha\text{-AlFeSi}$, and $\alpha\text{-Al(FeMn)Si}$ were reduced. The amount of needle-shaped Fe intermetallic phases, which are positioned at the tip of the $\alpha\text{-Al}$ phase and intermetallic compounds, is reduced, consequently, SDAS values increased [29].

As shown in **Table 1**, the area fraction of Si increased from $11.97\% (\pm 2.12\%)$ to $12.15\% (\pm 1.12\%)$ and from $12.18 (\pm 1.18\%)$ to $12.53 (\pm 2.01\%)$ for AlSi7Mg0.3 and AlSi10MnMg , respectively. Further, the Si sphericity of AlSi7Mg0.3 and AlSi10MnMg decreased from $0.805 (\pm 0.04)$ and $0.824 (\pm 0.02)$ to $0.795 (\pm 0.04)$ and $0.752 (\pm 0.03)$, respectively, after adding $\text{Na}_2\text{B}_4\text{O}_7$. This changed shape is inferred from the Ostwald ripening effects, wherein, the number of eutectic grains generating eutectic Si nucleation is increased due to $\text{Na}_2\text{B}_4\text{O}_7$. Therefore, the surface area between the liquid and solid is increased, consequently reducing the nucleation rate [30].

3.3 XRD analysis

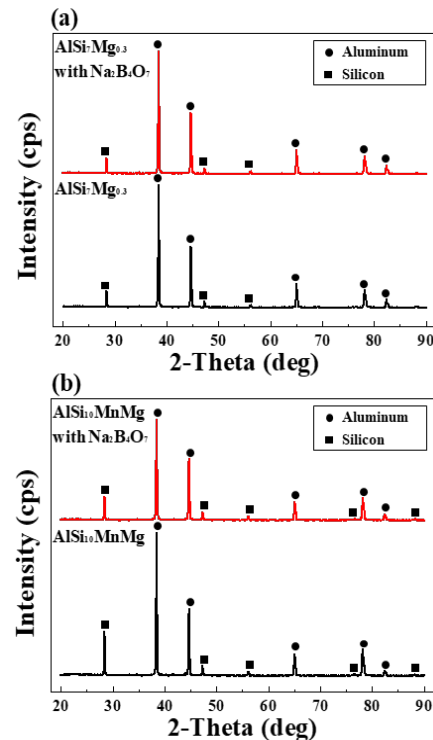


Figure 6: XRD patterns of as-cast AlSi7Mg0.3 , as-cast AlSi10MnMg , and alloys with the addition of $\text{Na}_2\text{B}_4\text{O}_7$

Figure 6 shows the XRD patterns of AlSi7Mg0.3 and AlSi10MnMg before and after the addition of $\text{Na}_2\text{B}_4\text{O}_7$. The

analysis confirmed that the main peaks of the detected crystalline phases were peaks of Al and Si in the Al-Si alloys. Because the intermetallic compounds observed using FE-SEM and EDS have a finer amount of precipitation than aluminum and silicon, they are present as background noise and were not detected as XRD peaks [31], and the XRD patterns of both AlSi7Mg0.3 with Na₂B₄O₇ and AlSi10MnMg with Na₂B₄O₇ alloys have no significant difference.

3.4 Porosity analysis

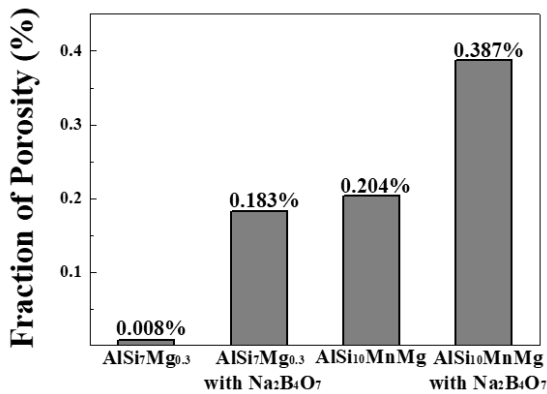


Figure 7: Porosity area fractions of as-cast AlSi7Mg0.3, as-cast AlSi10MnMg, and alloys with the addition of Na₂B₄O₇

Figure 7 shows the porosity area fraction of as-cast AlSi7Mg0.3, as-cast AlSi10MnMg and alloys with the addition of Na₂B₄O₇ by conducting a reduced pressure test. AlSi7Mg0.3 showed a porosity fraction of 0.008 %, and when Na₂B₄O₇ was added, the fraction increased by 0.17 % to a value of 0.183 % and that of AlSi10MnMg increased by 0.18 % from 0.204 % to 0.387 %. Hydrogen in both Na₂B₄O₇ and molten metal is dissolved in aluminum, and then supersaturated hydrogen molecules are formed between dendrites by exceeding the hydrogen solubility during solid-phase solidification in the liquid phase.

3.5 Tensile test and micro-hardness of aluminum alloy

Table 2 shows the changes in the tensile characteristics of alloys with the addition of Na₂B₄O₇. When Na₂B₄O₇ was added, the tensile strength of AlSi7Mg0.3 alloy decreased from 176.32 (± 16.8) MPa to 164.87 (± 7.15) MPa, and that of AlSi10MnMg alloy decreased from 195.11 (± 8.42) MPa to 183.33 (± 9.2) MPa. The yield strength of AlSi7Mg0.3 and AlSi10MnMg alloys reduced from 128.85 (± 6.77) MPa to 119.65 (± 5.49) MPa and from 131.16 (± 4.91) MPa to 126.67 (± 4.33) MPa, respectively. The tensile strength and yield strength were reduced after the

addition of Na₂B₄O₇ in both the alloys and the pore area fraction and widened SDAS increased after the addition of Na₂B₄O₇ as afore-mentioned. In the case of the elongation, AlSi7Mg0.3 had an elongation of 9.89 (± 1.56) %, and the elongation increased to 11.28 (± 0.85) % after the addition of Na₂B₄O₇. However, the elongation of AlSi10MnMg decreased from 15.76 (± 2.82) % to 14.06 (± 1.74) % after the addition of Na₂B₄O₇.

Table 2: Yield strength, tensile strength, and tensile strain of as-cast AlSi7Mg0.3, as-cast AlSi10MnMg, and alloys with the addition of Na₂B₄O₇

Tensile Property		Yield Strength (MPa)	Tensile Strength (MPa)	Tensile Strain (%)
Alloys				
AlSi7Mg _{0.3}	as-cast	128.85 (±6.77)	176.32 (±16.8)	9.89 (±1.56)
	with Na ₂ B ₄ O ₇	119.65 (±5.49)	164.87 (±7.15)	11.28 (±0.85)
AlSi10MnMg	as-cast	131.16 (±4.91)	195.11 (±8.42)	15.76 (±2.82)
	with Na ₂ B ₄ O ₇	126.67 (±4.33)	183.33 (±9.2)	14.06 (±1.74)

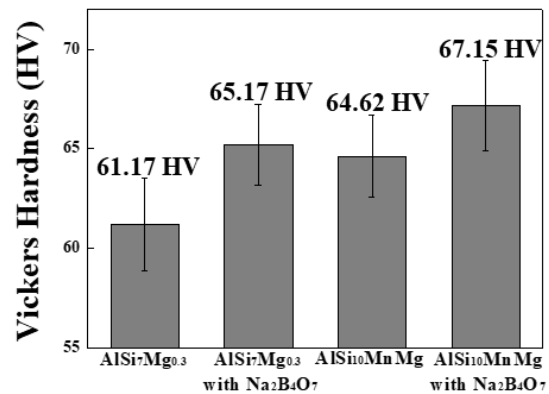


Figure 8: Micro-hardness results of as-cast AlSi7Mg0.3, as-cast AlSi10MnMg, and alloys with the addition of Na₂B₄O₇

Further, **Figure 8** shows that when Na₂B₄O₇ is added, the hardness characteristics of AlSi7Mg0.3 increased from 61.17 (±2.34) HV to 65.17 (±2.04) HV and that of AlSi10MnMg also increased from 64.62 (±2.07) HV to 67.15 (±2.25) HV, which are in contrast to the tensile strength results. Although the addition of Na₂B₄O₇·10H₂O causes high porosity, brittle and needle-shaped intermetallic compounds are converted into small intermetallic compounds or Chinese-script-shaped intermetallic compounds to increase the bonding strength with an Al matrix, thereby increasing the hardness value. This is caused by the decrease in the area fraction of Fe intermetallic compounds that negatively affect the hardness characteristics [32]-[33].

3.6 Fracture surface of aluminum alloy

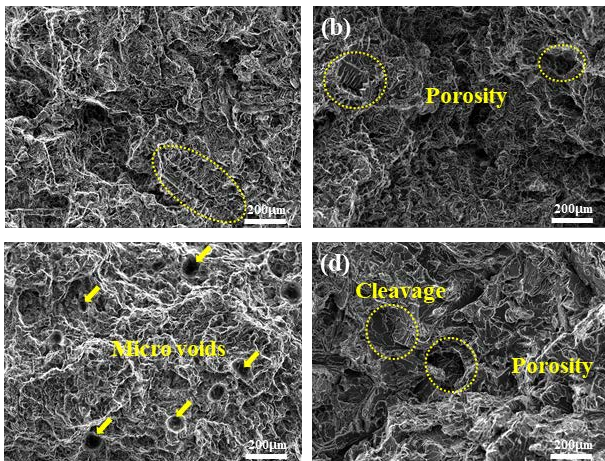


Figure 9: Fracture surfaces of (a) as-cast AlSi7Mg0.3, (c) as-cast AlSi10MnMg, (b) AlSi7Mg0.3 with Na₂B₄O₇, and (d) AlSi10MnMg with Na₂B₄O₇

Figure 9 shows the fracture surfaces of AlSi7Mg0.3 and AlSi10MnMg alloys after the tensile test, and all fracture surfaces contain dimple shapes and ductility failures, which are broken by micro-voids and primary Si particles, which is the main fracture mechanism [34]. As shown in **Figure 9**, fracture occur in the dendrite direction in AlSi7Mg0.3, and AlSi7Mg0.3 with Na₂B₄O₇ has dendrites inside the pores, which are microvoids in the form of shrinkage pores occurring during the phase shift of the solid. In other fracture locations, AlSi7Mg0.3 consisted of fracture of the eutectic Si particles and ductile fracture. In AlSi10MnMg, fracture occurred due to relatively larger and more voids than other alloys [34], and the AlSi10MnMg with Na₂B₄O₇ alloy fractured due to blocky Si, and cleavage fracture was observed near the pores.

4. Conclusion

Fe-rich intermetallics of π -Al₈Mg₃FeSi₆ and β -Al₅SiFe were observed in AlSi7Mg0.3, but small and fine intermetallic compounds were observed after Na₂B₄O₇ addition. Although α -Al₁₅(Fe,Mn)Si₂ and eutectic Si particles were observed in AlSi10MnMg, the needle-shaped α -Al₁₅(Fe,Mn)Si₂ transformed to Chinese-script-shaped α -Al₁₅(Fe,Mn)Si₂ with the addition of Na₂B₄O₇. Further, the SDAS of AlSi7Mg0.3 increased to 3.82 μ m after the addition of Na₂B₄O₇, and that of AlSi10MnMg increased to 2.69 μ m. The Fe intermetallic phase fraction of AlSi7Mg0.3, as-cast AlSi10MnMg alloys decreased by 0.17 % and 0.15 %, respectively, despite the addition of Na₂B₄O₇ with

maximum hydrogen solubility. The tensile strength and yield strength of the AlSi7Mg0.3 with Na₂B₄O₇ alloy decreased to 11.45 MPa and 9.2 MPa, and those of AlSi10MnMg with Na₂B₄O₇ decreased to 11.78 MPa and 4.5 MPa, respectively. However, when Na₂B₄O₇ was added, the elongation of AlSi7Mg0.3 and AlSi10MnMg alloys increased by 1.34 % and decreased by 1.7 %, respectively. Despite the decrease in the tensile values, the hardness values of AlSi7Mg0.3 and AlSi10MnMg increased by 4 HV and 2.53 HV when Na₂B₄O₇ was added. Therefore, the Na₂B₄O₇ in the alloys functions as a flux and in addition generates a microstructure control effect, suggesting the prospect of Na₂B₄O₇-based applications.

Acknowledgement

This research was supported by the National Research Foundation of Korea (NRF) granted by the Korean Government (NRF-2019R111A3A01062863).

Author Contributions

Conceptualization, J. Bang and E. Lee; Methodology, J. Bang; Software, J. Bang; Validation, J. Bang, E. Byon and E. Lee; Formal Analysis, J. Bang; Investigation, J. Bang; Resources, J. Bang; Data Curation, J. Bang; Writing—Original Draft, Preparation, J. Bang; Writing—Review & Editing, E. Byon and E. Lee; Visualization, J. Bang; Supervision, E. Lee; Project Administration, E. Lee; Funding Acquisition, E. Lee. All authors have read and agreed to the published version of the manuscript.

References

- [1] T. H. G. Megson, *Introduction to Aircraft Structural Analysis*, 3rd edition, Oxford, United Kingdom: Butterworth-Heinemann, 2018.
- [2] G. Moon and E. Lee, "Combined effects of optimized heat treatment and nickel coating for the improvement of interfacial bonding in aluminum–iron alloys hybrid structures," *Applied Sciences*, vol. 11, no. 4, p. 1501, 2021.
- [3] M. Wang, D. H. Xiao, and W. S. Liu, "Effects of Si addition on microstructure and properties of magnesium alloys with high Al and Zn contents," *Vacuum*, vol. 141, pp. 144-151, 2017.
- [4] S. O. Adeosun, S. A. Balogun, L. O. Osoba, W. A. Ayoola, and A. M. Oladoye, "Effects of Cu and Zn addition on the mechanical properties of structural aluminum alloy," *Manufacturing Technology*, vol. 3, pp. 103-110, 2011.

- [5] N. Yass and K. Nagham, "Study the effects of magnesium addition on microstructure, electrical conductivity and some mechanical properties of pure aluminum," *Journal of Babylon University, Engineering Sciences*, vol. 25, no. 1, pp. 251-260, 2017.
- [6] H. R. Ammar, A. M. Samuel, and F. H. Samuel, "Porosity and the fatigue behavior of hypoeutectic and hypereutectic aluminum–silicon casting alloys," *International Journal of Fatigue*, vol. 30, no. 6, pp. 1024-1035, 2008.
- [7] L. Lu and A. K. Dahle, "Iron-rich intermetallic phases and their role in casting defect formation in hypoeutectic Al-Si alloys," *Metallurgical and Materials Transactions A*, vol. 36, pp. 819-835, 2005.
- [8] J. A. Taylor, "Iron-containing intermetallic phases in Al-Si based casting alloys," *Procedia Materials Science*, vol. 1, pp. 19-33, 2012.
- [9] Q. G. Wang, D. Apelian, and D. A. Lados, "Fatigue behavior of A356-T6 aluminum cast alloys. Part I. Effects of casting defects," *Journal of Light Metals*, vol. 1, no. 1, pp. 73-84, 2001.
- [10] C. H. Cáceres and B. I. Selling, "Casting defects and the tensile properties of an AlSiMg alloy," *Materials Science and Engineering: A*, vol. 220, no. 1-2, pp. 109-116, 1996.
- [11] B. Li, Y. Shen, and W. Hu, "Casting defects induced fatigue damage in aircraft frames of ZL205A aluminum alloy – A failure analysis," *Materials & Design*, vol. 32, no. 5, pp. 2570-2582, 2011.
- [12] J. R. Davis, *Aluminum and Aluminum Alloys*, ASM International, United States of America, 2001.
- [13] J. W. Gao, D. Shu, J. Wang, and B. D. Sun, "Effects of Na₂B₄O₇ on the elimination of iron from aluminum melt," *Scripta Materialia*, vol. 57, no. 3, pp. 197-200, 2007.
- [14] J. W. Gao, D. Shu, J. Wang, and B. D. Sun, "Study on iron purification from aluminium melt by Na₂B₄O₇ flux," *Materials Science and Technology*, vol. 25, no. 5, pp. 619-624, 2009.
- [15] M. A. Moustafa, "Effects of iron content on the formation of β-Al₅FeSi and porosity in Al–Si eutectic alloys," *Journal of Materials Processing Technology*, vol. 209, no. 1, pp. 605-610, 2009.
- [16] N. Vanderesse, É. Maire, A. Chabod, and J. -Y. Buffière, "Microtomographic study and finite element analysis of the porosity harmfulness in a cast aluminium alloy," *International Journal of Fatigue*, vol. 33, no. 12, pp. 1514-1525, 2011.
- [17] J. Lee, Y. Jeong, D. Shim, and E. Lee, "Microstructural evolution and martensitic transformation in FeCrV alloy fabricated via additive manufacturing," *Materials Science and Engineering: A*, vol. 809, pp. 140943, 2021.
- [18] J. E. Gruzleski and B. M. Closset, "The treatment of liquid aluminum–silicon alloys," *American Foundrymen's Society, Des Plaines*, 1990.
- [19] G. S. Cho and K. H. Choe, "Study on the rationalization of aluminium casting alloys for automobiles components," *Journal of the Korea Foundry Society*, vol. 31, no. 6, pp. 319-325, 2011 (in Korean).
- [20] I. Jo, C. Ahn, and E. Lee, "High-temperature tensile deformation behavior and failure mechanisms of Al-10Si-Mn-Mg high-pressure die-cast alloy," *Journal of Advanced Marine Engineering and Technology*, vol. 43, no. 10, pp. 788-792, 2019.
- [21] H. S. Chul and S. Y. Kwak, "Effects of shrinkage defect on fracture impact energy of A356 cast aluminum alloy," *Journal of Korea Foundry Society*, vol. 34, no. 1, pp. 22-26, 2014 (in Korean).
- [22] J. Lazaro-Nebreda, J. B. Patel, and Z. Fan, "Improved degassing efficiency and mechanical properties of A356 aluminium alloy castings by high shear melt conditioning (HSMC) technology," *Journal of Materials Processing Technology*, vol. 294, pp. 117146, 2021.
- [23] M. Wang, W. Xu, and Q. Han, "Effects of heat treatment on controlling the morphology of AlFeSi Phase in A380 alloy," *International Journal of Metalcasting*, vol. 10, no. 4, pp. 516-523, 2016.
- [24] J. G. Conley, J. Huang, J. Asada, and K. Akiba, "Modeling the effects of cooling rate, hydrogen content, grain refiner and modifier on microporosity formation in Al A356 alloys," *Materials Science and Engineering: A*, vol. 285, no. 1-2, pp. 49-55, 2000.
- [25] J. Wisniak, "Borax, boric acid, and boron - From exotic to commodity," *Indian Journal of Chemical Technology*, vol. 12, no. 4, pp. 488-500, 2005.
- [26] G. A. Mengesha, J. P. Chu, B. -S. Lou, and J. -W. Lee, "Effects of processing parameters on the corrosion performance of plasma electrolytic oxidation grown oxide on commercially pure aluminum," *Metals*, vol. 10, no. 3, p. 394, 2020.

- [27] L. Qiyang, L. Qingchun, and L. Qifu, "Modification of Al-Si alloys with sodium," *Acta Metallurgica et Materialia*, vol. 39, no. 11, pp. 2497-2502, 1991.
- [28] H. D. Alamdari, D. Dubé, and P. Tessier, "Behavior of boron in molten aluminum and its grain refinement mechanism," *Metallurgical and Materials Transactions A*, vol. 44, pp. 388-394, 2013.
- [29] B. H. Kim, J. K. Kim, and S. M. Lee, "Magnetic separation of Fe contaminated Al-Si cutting chip scraps and evaluation of solidification characteristics," *Journal of the Korean Foundrymen's Society*, vol. 29, no. 1, pp. 38-44, 2009 (in Korean).
- [30] J. Fu, S. Wang, and K. Wang, "Influencing factors of the coarsening behaviors for 7075 aluminum alloy in the semi-solid state," *Journal of Materials Science*, vol. 53, pp. 9790-9805, 2018.
- [31] M. H. Yoo, K. W. Kim, and M. S. Moon, "A study on mechanical properties according to changes in microstructure and precipitation phase of A356 alloy and the Mn and the St added to A356 alloy," *Journal of the Korean Society of Mechanical Technology*, vol. 22, no. 4, pp. 740-746, 2020 (in Korean).
- [32] S. G. Irizalp and N. Saklakoglu, "Effect of Fe-rich intermetallics on the microstructure and mechanical properties of thixoformed A380 aluminum alloy," *Engineering Science and Technology, an International Journal*, vol. 17, no. 2, pp. 58-62, 2014.
- [33] Y. Zedan, F. H. Samuel, A. M. Samuel, and H. W. Doty, "Effects of Fe intermetallics on the machinability of heat-treated Al-(7-11) % Si alloys," *Journal of Materials Processing Technology*, vol. 210, no. 2, pp. 245-257, 2010.
- [34] C. Ahn, I. Jo, C. Ji, S. Cho, B. Mishra, and E. Lee, "Creep behavior of high-pressure die-cast AlSi10MnMg aluminum alloy," *Materials Characterization*, vol. 167, 110495, 2020.